Quarterly Journal of the Royal Meteorological Society *Q. J. R. Meteorol. Soc.* 138: 1–14 (2013)

An analysis of the observed low-level structure of rapidly intensifying and mature Hurricane Earl (2010)

Michael T. Montgomery[a]*, Jun A. Zhang[b], and Roger K. Smith[c]
[a] *Dept. of Meteorology, Naval Postgraduate School, Monterey, CA, USA*
[b] *NOAA Hurricane Research Division, Miami, FL, USA*
[c] *Meteorological Institute, University of Munich, Munich, Germany*
*Correspondence to: Prof. Michael T. Montgomery, Dept. of Meteorology, Naval Postgraduate School, Monterey, CA 93943, USA. E-mail: mtmontgo@nps.edu

We examine dynamic and thermodynamic aspects of Atlantic Hurricane Earl (2010) during its intensification and mature phases over four days of intensive measurements. During this period, Earl underwent an episode of rapid intensification, maturity, secondary eyewall replacement, re-intensification and early decline. The observations are used to appraise elements of a new model for tropical-cyclone intensification.

Key Words: Hurricanes, typhoons, conventional spin-up mechanism, boundary layer spin-up mechanism, thermodynamic structure, surface enthalpy fluxes, GRIP

Received March 3, 2013; Revised ; Accepted

Citation: ...

1. Introduction

Early theories of tropical-cyclone intensification emphasized the role of deep convective clouds, which, in an azimuthally-averaged sense, generate radial convergence in the low to mid-troposphere (Charney and Eliassen 1964, Ooyama 1964). These authors showed that spin up was a result of the accompanying import of absolute angular momentum, M, above the frictional boundary layer, where M is materially conserved. Here $M = rv + 1/2fr^2$, where r denotes radius from storm centre, v denotes azimuthally-averaged, storm-relative tangential velocity and f denotes the Coriolis parameter.

Dissatisfied by thermodynamical aspects of the foregoing studies, Ooyama formulated a highly simplified three-layer slab model with an entraining-plume representation of deep convection on the vortex scale and of sensible and latent heat fluxes from the underlying ocean (Ooyama 1969). As in the earlier models, the spin up was associated with the convectively-induced import of M, but that spin up required a supply of latent heat energy from the ocean to maintain the (parameterized) deep convection. We will refer to the convectively-induced import of M above the boundary layer, in conjunction with the supply of moisture from the underlying ocean surface, as the conventional intensification model (Ooyama 1969, 1982, Willoughby 1988, 1995).

A seemingly different model for spin up was proposed by Emanuel (1997) that focussed more on the thermodynamic controls on the intensification process, but as noted by Montgomery and Smith (2013), the dynamical mechanism for spin up appears to be again the radial import of M above the frictional boundary layer by deep convection. An appraisal of these early paradigms for tropical-cyclone intensification, all of which are axisymmetric, together with a new three-dimensional one is given by Montgomery and Smith *op. cit.*

A new paradigm for tropical-cyclone intensification has been expounded in a series of recent papers (Nguyen *et al.* 2008, Montgomery *et al.* 2009, Smith *et al.* 2009, Bui *et al.* 2009) and summarized by Montgomery and Smith (2013). This paradigm was distilled from the results of the foregoing studies using observations and high-resolution, three-dimensional, numerical model simulations that represent deep convection explicitly and recognizes the role of rotating deep convection in the spin-up process. Analyses of azimuthally-averaged fields in the foregoing simulations lead to a revised view of spin up that includes the conventional intensification mechanism, but emphasizes the important *dynamical role* of the boundary layer. In fact,

Smith *et al.* (2009) showed that the spin up of the maximum tangential winds takes place *within* the frictional boundary layer, although the spin up of the winds above the boundary layer is necessary as well. (A similar result was noted by Zhang *et al.* (2001) in a simulation of Hurricane Andrew (1992), but they did not appear to recognize the generality of their result.) As in the earlier paradigms, the spin up of the bulk vortex above the boundary layer occurs through the conventional mechanism as discussed above.

The boundary-layer spin up mechanism may seem counter-intuitive to those who have studied boundary layers only in the context of nonrotating flows, where friction reduces the flow near the boundary. The mechanism is possible because the inward displacement of air parcels is much larger in the boundary layer than above, a consequence of the frictional disruption of gradient wind balance that holds approximately above the boundary layer. This disruption leads to a net inward force in the boundary layer. Since the azimuthal mean tangential wind speed $v = M/r - \frac{1}{2}fr$, the possibility arises that the loss of M to the surface following an air parcel may be more than offset by a large inward displacement of the air parcel so that the tangential wind increases, eventually becoming larger than that above the boundary layer. In high resolution model simulations, the process is exemplified by time-height cross-sections of the azimuthally-averaged M-surfaces, which tilt inwards with height within the boundary layer and outwards with height above with a "nose" at the top of the strong inflow layer. While there have been observations of such nose-like structures in a mature hurricane (e.g. Bell and Montgomery 2008), to our knowledge the evolution of the M-surfaces during intensification has not been reported for an intensifying tropical cyclone.

In a nutshell, on the system-scale, the new spin up paradigm has two dynamical components. The first is the conventional spin up mechanism, i.e., convectively-induced inflowing rings of air in the lower troposphere that approximately materially conserve their M. The second component comprises the boundary-layer spin-up mechanism summarized in the foregoing discussion. A related and essential ingredient of the new spin up paradigm is the maintenance of convective instability in the inner-core region of the vortex as discussed above.

Although the focus of the present study is on the low-level structure of both the intensification and mature phases of a hurricane, some aspects of Emanuel's steady-state hurricane model (Emanuel 1986, henceforth E86) still provide a useful context for interpreting observations of an intensifying storm. An important feature of this model is the assumption that as air parcels ascend along the eyewall, they conserve their absolute angular momentum, M, and saturation pseudo-equivalent potential temperature, θ_e^*, so that M and θ_e^* surfaces are congruent. In addition, the theory assumes explicitly that the tangential flow above the boundary layer is in gradient wind balance. An important constraint in the model is the rate at which M and θ_e^* vary with radius in the boundary layer inside the radius of maximum tangential wind speed (r_m), which E86 assumes to be located at the outer edge of the eyewall (see E86, Figure 1). A brief summary of the model formulation is contained in section 2 of Smith *et al.* (2008). While the model has undergone a number of reincarnations over the years (Emanuel 1988, Emanuel 1995, Bister and Emanuel 1998, 2002, Emanuel 2004, Emanuel and Rotunno 2011), the foregoing aspects have remained unchanged.

An important feature of the E86 model is the increase in θ_e^* with diminishing radius in the vicinity of the eyewall updraught. Such a feature had been documented earlier from observational analyses (Hawkins and Imbembo 1976) and has been confirmed by more recent work (Montgomery *et al.* 2006, Marks *et al.* 2008, Bell and Montgomery 2008). Since the virtual temperature, θ_v, in cloud increases monotonically with θ_e^*, θ_v must increase also with decreasing radius at a given pressure level, consistent with the warm core structure of the vortex. Because ascending air parcels move to larger radii, the M and θ_e^* surfaces flare outwards with height. As these air parcels move outwards conserving M they spin more slowly about the rotation axis of the storm, which, together with the positive radial gradient of M, explains the observed decrease of the tangential wind speed with height, consistent with the thermal wind equation (E86). As discussed by Montgomery and Smith (2013), in the new intensification paradigm, only modest surface moisture fluxes are required from the underlying ocean, which give rise to an increase of boundary layer θ_e with decreasing radius. The θ_e increase is needed to help maintain a degree of convective instability of the inner-core region in the presence of a developing warm core aloft. This increase does not necessarily require an evaporative-wind feedback process as hypothesized by Emanuel *et al.* (1994) and Emanuel (2003). In fact, Montgomery *et al.* (2009) have shown that this evaporative-wind feedback mechanism is neither essential nor the dominant pathway for tropical cyclone spin up.

Observational support of the second spin-up mechanism for tropical cyclone intensification was presented by Sanger (2011) and Sanger *et al.* (2013) who examined the boundary layer structure during the intensification of typhoon Jangmi, which was observed as part of the Tropical-Cyclone - Structure 2008 (TCS08) experiment (Elsberry and Harr 2008). An even more detailed data set for testing this spin-up mechanism and the new intensification paradigm was obtained in Hurricane Earl (2010) during four days of intensive measurements based on airborne dropwind-sondes released from the upper troposphere during the collaborative National Aeronautics and Space Administration (NASA), Genesis and Rapid Intensification Processes (GRIP) and the National Oceanic and Atmospheric Administration (NOAA), Intensity and Foreasting Experiment (IFEX). Here we examine dynamic and thermodynamic kinematic and thermodynamic structure of this Atlantic hurricane during its intensification and mature phases. During the extensive observation period, Earl underwent one episode of rapid intensification and the measurements afford a unique opportunity to assess several aspects of the new paradigm of tropical cyclone intensification. They afford also the possibility of extending the analysis of Smith and Montgomery (2013a) to quantify the changes in the radial distribution of boundary-layer θ_e as the storm intensifies.

The paper is organized as follows. In section 2 we give a brief summary of Hurricane Earl, focussing largely on the period from rapid intensification to maturity. In section 3 we summarize the data quality and analysis methodology employed. Sections 4 and 5 present the analysis of the observational data. Section 6 presents a summary of the main findings and discusses some implications of the results.

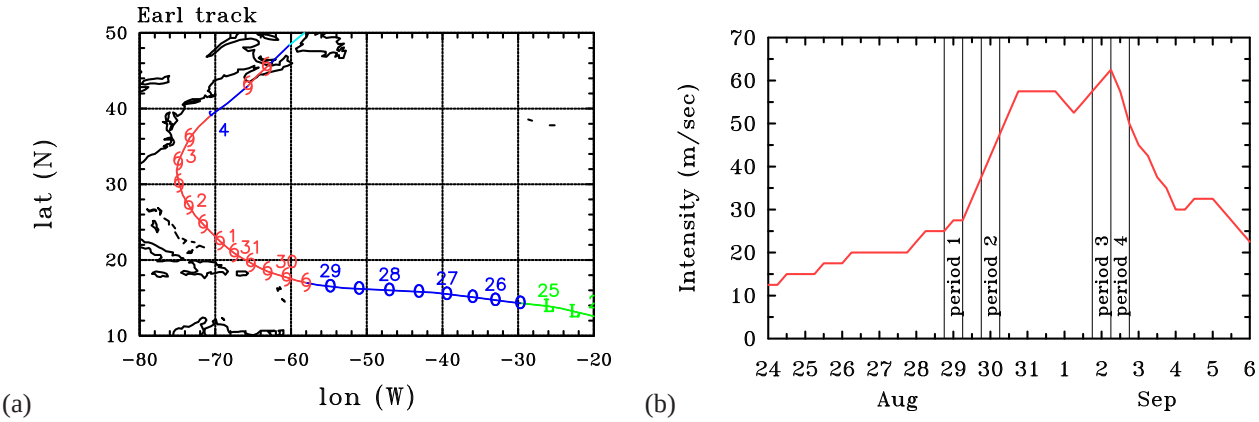

Figure 1. (a) Best track positions, and (b) intensity for Hurricane Earl, 25 August - 4 September 2010. Based on "best track" data from the National Hurricane Center archive. Vertical lines in (b) delineate four periods of flight reconnaissance referred to in the text.

2. Hurricane Earl and data collected

Hurricane Earl originated from a strong tropical wave that left the west coast of Africa on 23 August. The "best track" chart of Earl's path is given in Figure 1a, with the time series of its intensity shown in Figure 1b. The following description is based on the storm summary produced by the National Hurricane Center.

Strong subtropical ridging over the eastern Atlantic steered Earl westwards to west-north-westwards at a speed of between 7.5 and 10 m s^{-1} for the next few days. At the same time, the tropical storm strengthened gradually over a sea surface temperature of 28-29C and in an environment of light to moderate vertical shear. Data from an Air Force Reserve reconnaissance aircraft indicate that Earl became a hurricane by 1200 UTC [1] 29 August, when centred about 220 n mi east of the northern Leeward Islands. Around that time, Earl neared a weakness in the subtropical ridge associated with Hurricane Danielle to its west, and it slowed and gradually turned northwestward while undergoing rapid intensification. Earl strengthened to a Category 3 hurricane about 12 h later when it was located very near the northern Leeward Islands. Data from both NOAA and Air Force hurricane hunter aircraft, along with satellite imagery, indicate that Earl intensified by 40-kt over 24 h, becoming a Category 4 hurricane by 1800 UTC 30 August.

Figure 2 shows a composite reflectivity from the lower-fuselage (5 cm) radar on the NOAA P3 aircraft during four missions into the intensifying storm. The reflectivity image centred at 2250 UTC 28 August shows a cyclonically curved band of high reflectivity (exceeding 40 dBZ) that extends from the southwest to the east of the centre. At this time the eye, which is marked in the centre by very low reflectivity values (below 15 dBZ), has an approximately oval shape with diameter of 60 km in the east-west direction and 80 km in the north-south direction. By 1040 UTC 29 August the eye boundary has become more circular and the reflectivity pattern become a little more symmetric about the centre. During the next 12 hours the eye region has contracted and remains approximately symmetric with a final diameter of approximately 50 km. at 2200 UTC 29 August. Again, the reflectivity pattern has become asymmetric with two prominent reflectivity bands wrapping cycloncally inwards on the southeastern side of the centre. It is during this interval that the vortex intensifies rapidly (cf. Figure 1b). After another 12 hours by 1230 UTC 30 September the eye has contracted further and is almost surrounded by a narrow region of high reflectivity, characterizing a developing eyewall. The reflectivity of this eyewall is most extensive in the southeast sector. The bands of high reflectivity in the previous image have disappeared. A moat of low reflectivity is apparent mainly on the western and southwestern sides of the eye. The intensity at this time is approximately 55 m s^{-1}.

Subsequently, Earl began a concentric eyewall replacement cycle that was well observed in both the San Juan Doppler radar and aircraft flight level wind data. This cycle halted the intensification process and Earl remained a 115-kt hurricane for the next 24 h. Southwesterly shear increased late on 31 August, which resulted in Earl weakening back to a Category 3 hurricane by 0000 UTC 1 September. Earl weakened a little more during the morning hours of 1 September. However, by that afternoon the eye became more distinct and deep convective activity increased and gained symmetry, presumably due to a decrease in vertical shear. Earl re-intensified to Category 4 strength by 1800 UTC 1 September and reached its peak intensity of 63 m s^{-1} 12 h later, when it was located about 380 n mi southeast of Wilmington, North Carolina. An infrared satellite image of Earl near its peak intensity is shown in Figure 3. Earl then rapidly weakened as it turned northwards, falling below major hurricane status by 0000 UTC 3 September.

3. Data quality and analysis methodology

Hurricane Earl was extensively sampled by multiple research and reconnaissance aircraft from NOAA, NASA and the United States Air Force prior to, during, and at the end of the period of rapid intensification, with less than 12 h between sampling times for the inner core and less than 24 h for the environment. This represents one of most intensively-sampled lifecycles of rapid intensification ever. In our analyses, we use the Global Positioning System (GPS) dropwindsonde (henceforth dropsonde) data collected in Hurricane Earl between 28 August and 2 September, 2010. As an example, Figure 4 shows the dropsonde data coverage relative to the storm centre obtained from four different research aircraft. The position of each dropsonde shown corresponds to the position when the dropsonde was first released, but analyses in the forthcoming section use the instantaneous position of the

[1] Universal Time Coordinated

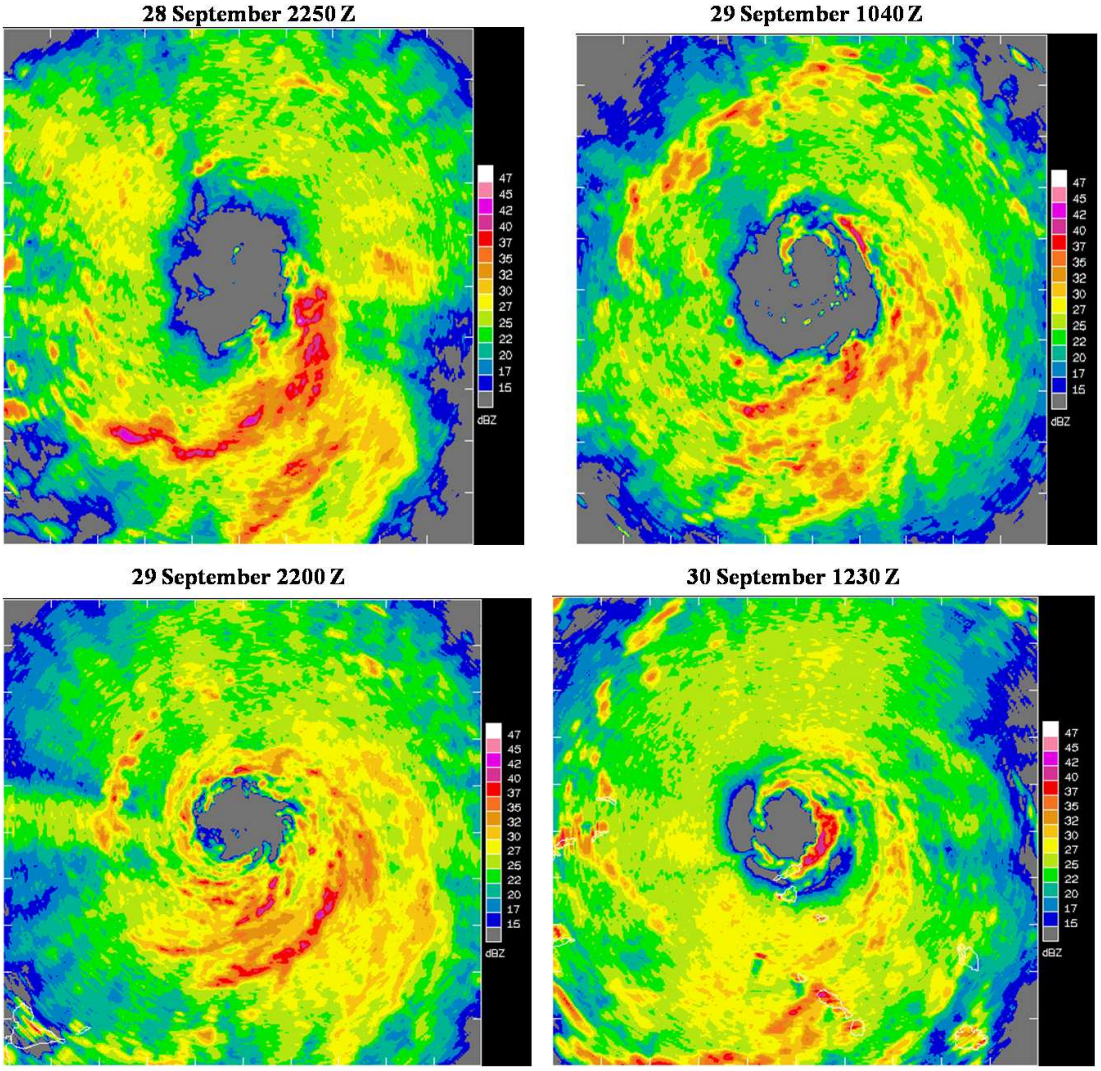

Figure 2. The reflectivity field as viewed by the lower fuselage radar of the WP-3D aircraft at (a) 2250 UTC 28 September, (b) 1040 UTC 29 September, (c) 2200 UTC 29 September, and (d) 1230 UTC 30 September. All four panels are 360 km x 360 km. The colour bar shows values in ranges of dBZ.

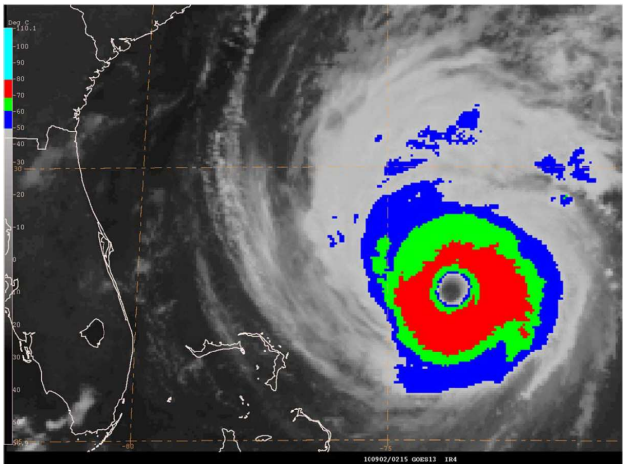

Figure 3. An infrared satellite image at 0215 UTC 2 September 2010 of Hurricane Earl near its peak intensity.

dropsonde at a particular height. We group the data into 12 hour windows to increase the sample size and focus on four periods, two during the period of rapid intensification (18 UTC 28 August to 6 UTC 29 August (period 1); and 18 UTC 29 August to 6 UTC 30 August (period 2) and two in which Earl had reached a quasi-steady state (18 UTC 1 September to 6 UTC 2 September (period 3); and 6 UTC 2 September to 18 UTC 2 September (period 4)). These four periods are indicated in Figure 1b.

All the dropsonde data were quality controlled using the ASPEN software, which is based on the EDITSONDE software developed by the Hurricane Research Division (Franklin et al. 2003). A standard 10 s filter is used to smooth turbulent noise and switching between GPS satellites, as in Powell (2003). A more detailed description of the observational instruments inside the dropwindsonde can be found in Hock and Franklin (1999). The accuracy of the horizontal wind speed measurements is 2.0 m s^{-1} and < 0.5 m s^{-1} for the vertical winds with approximately 0.2 m s^{-1} precision. The storm centre is determined using the flight-level data using the Willoughby and Chelmow (1982) method along with the best track record.

The radial and tangential components are computed relative to the instantaneous storm centre. We averaged the data located within the eyewall region, and found the height of the maximum mean tangential wind speed. To calculate the gradient wind at this height, we first fit the pressure data as a function of the radius from the storm centre. We next

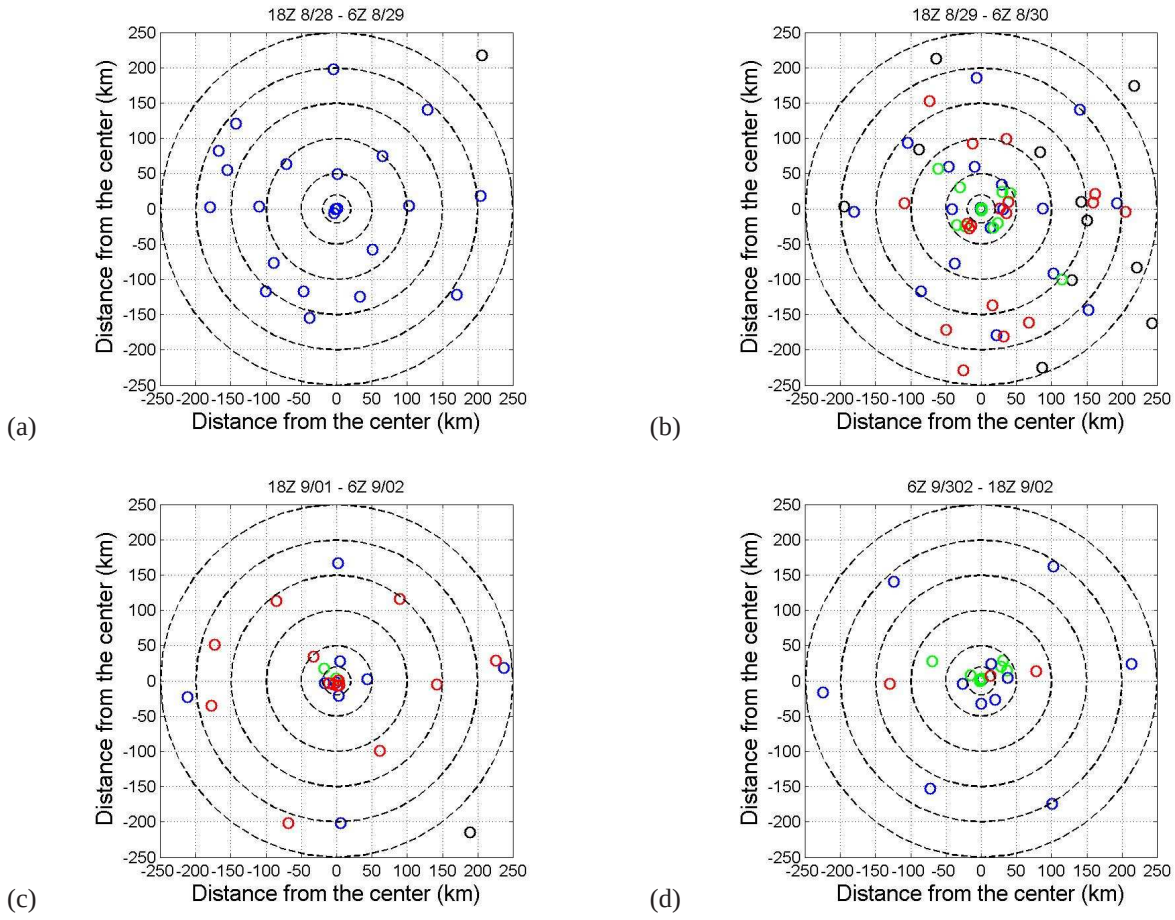

Figure 4. Storm-centred dropsonde distribution on the five days of monitoring of Earl by four different research aircraft. Each color represents one type of aircraft where dropondes were released. Blue color represents WP-3D aircraft, red color represents DC-8 aircraft, green color represents C-130 aircraft, black color represent G-IV aircraft. For simplicity, the storm-relative horizontal trajectory of each dropsonde after release time is not shown.

calculate the gradient wind by solving the quadratic gradient wind equation for tangential velocity using the inferred radial pressure gradient force (Eq. (1) below). Using this methodology, the radial profile of the mean gradient wind can then be compared with the local tangential wind speed at the same level (see e.g., Figures 11, 12 later).

4. Doppler-radar analysis and results thereof

The tail Doppler radar data from NOAAs WP-3D aircraft are used to construct storm-centred r-z plots of M for each flight. Such plots are then used to assess the first component of the new intensification paradigm of Montgomery and Smith (2013), in which the conventional intensification mechanism for the system-scale circulation discussed in the Introduction is an important element.

The data are processed as follows. An automated quality control process is applied before the data analysis (Gamache 2012). The fore/aft scanning technique is used to create dual-Doppler measurements from a single radial penetration (e.g., Reasor *et al.* 2009). The Doppler radar projection equations and anelastic mass continuity equation are solved at the same time to derive the three-dimensional wind field via least-squares minimization (Gamache 1997). The quality-controlled Doppler radials extend from the surface to 20 km with horizontal and vertical grid spacings of 2 km and 0.5 km, respectively. The vortex centre is defined using a modified version of the centre-finding method of Marks *et al.* (1992) as detailed by Reasor and Eastin (2012).

To determine the distribution of azimuthally-averaged M, analyses from individual radial penetrations during each flight are first merged. The purpose for merging radar swaths is to create the most complete azimuthal coverage of the core region out to the largest radius. A detailed description of the methodology used for merging the swaths and its limitations are given by Reasor *et al.* (2013). The radar data are observed mainly above 500 m, so that most of the data are above the boundary layer.

Figure 5 shows the evolution of M surfaces as calculated from the merged Doppler radar data for each flight. Note that, in calculating M, we use a constant f for each flight. The value of f is calculated using the averaged latitude of the moving storm centre for each flight. As the storms move during the period of eyewall penetrations, we have assumed that structural features of interest are quasi-steady over the observation period. Because the latitude change in the storm centre is small (< 0.6 deg) during the period of eyewall penetrations for each flight, the change in f associated with the moving storm is very small which ($<$ 3%), implying a negligible change of the M fields over the Doppler radar domain shown. It is evident from the figure that M increases with radius at each level during the spin-up process of Hurricane Earl, implying that the vortex is centrifugally (or inertially) stable (e.g., Shapiro and Montgomery 1993, Franklin *et al.* . 1993) and that the mean radial inflow can carry high M air to the centre to spin up the tangential wind field there. We see also that, indeed, over the period of observations, the M surfaces

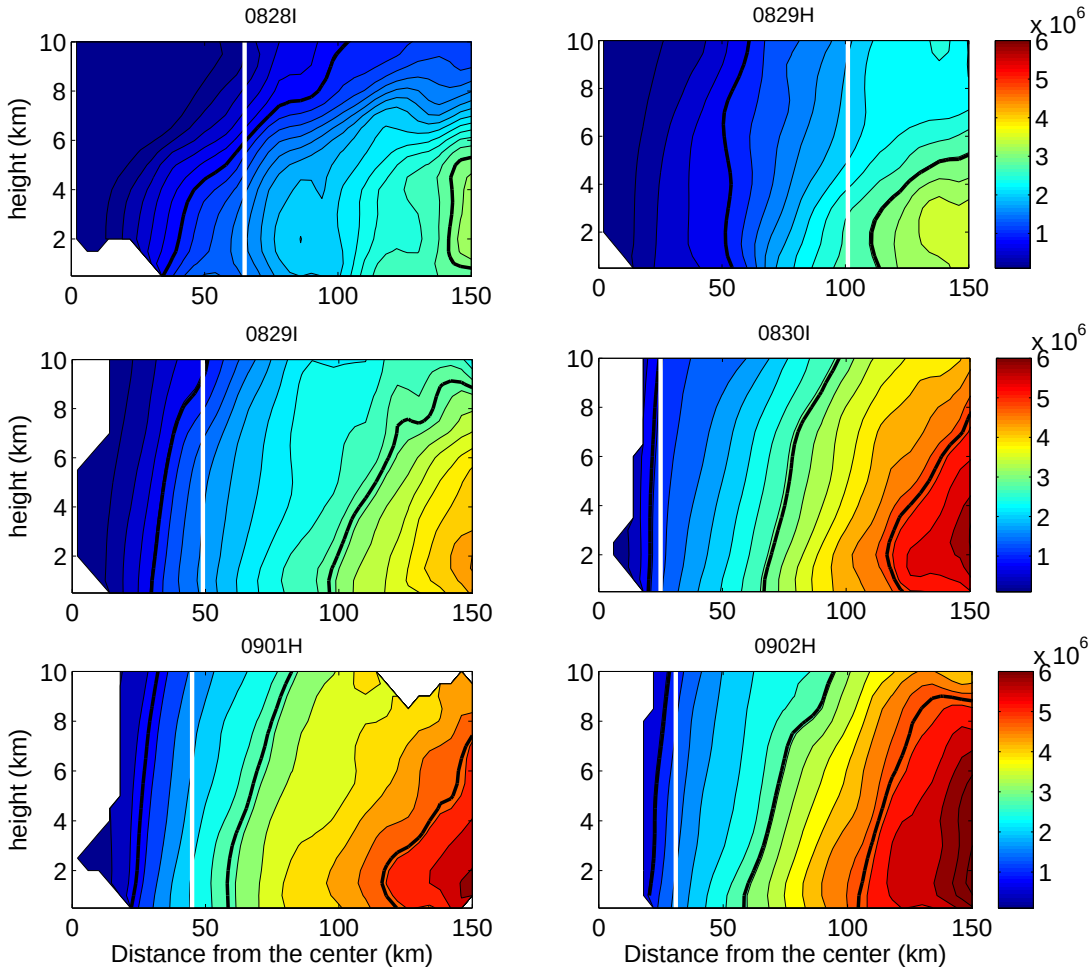

Figure 5. Evolution of absolute angular momentum, M, which is azimuthally-averaged about the storm centre. These M-data are from Doppler radar and dropwindsondes as discussed in section 4. The panels show only the deep tropospheric data above 500 m altitude. The radius of maximum azimuthally-averaged tangential velocity at 1 km altitude is indicated by the white vertical line in each panel.

do move radially inwards. Moreover, the signature of the strengthening boundary layer inflow is evident by the increase in the upward-outward tilt of the M surfaces in the lower troposphere as these surfaces move inwards. The dark solid curves are chosen to highlight a few M surfaces during the rapid intensification phase of the vortex. As an example, in the top-left panel of curve in Figure 5 (0828I, corresponding to 28 August), there are two particular M surfaces identified. The innermost M surface begins near 50 km radius (the edge of the inner Doppler-radar data region on this day) and slopes outwards and upwards to 10 km height and 100 km radius. In subsequent panels, this surface becomes more upright and moves inwards to near 25 km radius, where the eyewall has developed and the Doppler radar data are adequate to apply the analysis methodology. At outer radii, a qualitatively similar evolution is observed. The second M surface highlighted in the top-left panel of Figure 5 is seen initially near 140 km radius and during the next 48 h hours extends vertically and moves inwards to approximately 70 km radius on 30 August (panel 0830I). A similar picture is found with the third M surface that enters the domain by 30 August near 125 km (panel 0830I). Over the next three days, this third M surface moves inwards approximately 20 km and extends vertically. In summary, the M surfaces are found to be moving inwards during the period of observations. Although there is some tendency of the M surfaces to bow inwards near 2 km altitude outside of the RMW, we are cautious of attributing much significance to this feature on account of the difficulty of extracting Doppler data at low altitudes.

5. Dropwindsonde analysis and results

5.1. Spin up in the boundary layer

To assess the boundary-layer spin-up mechanism, we study next the boundary layer structure using the dropsonde data with a focus on below 2 km altitude in the vicinity of the high wind region of the vortex. Figure 6 shows an example of the dropwindsone wind data at a level of 1 km obtained during period 1, an interval sampling the rapid intensification period (cf. Figure 1b). The Doppler-radar derived wind field (described in the foregoing section) are shown at the same level and time period. The figure broadly supports the assumption that the horizontal wind field in the high-wind region possesses a fair degree of symmetry during this period. Similar figures during the other periods have been constructed (not shown) and together they imply that the composite methodology employed herein should provide a meaningful estimate of the azimuthally-averaged vortex structure.

Figures 7-10 display the individual and composite vertical profiles of storm-relative tangential (V_t) and radial (V_r) wind velocities in the eyewall region for the four

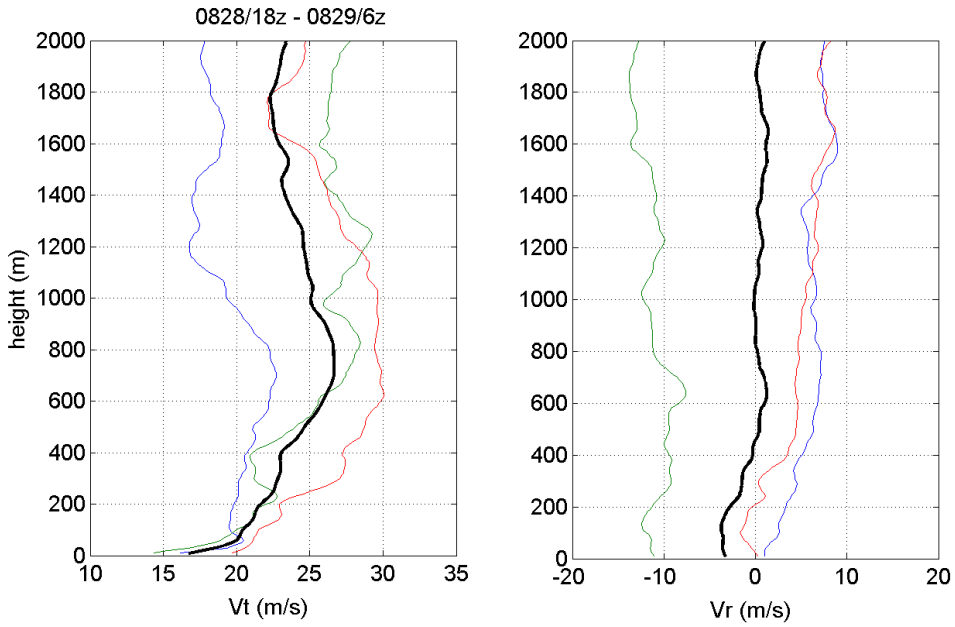

Figure 7. Vertical profiles of storm-relative tangential (V_t) and radial (V_r) wind composites and deviations thereto in the eyewall region of the vortex during the period 1: 0828/18Z - 0829/06Z. The eyewall region is defined as the region within 10 km from the RMW deduced using the Dopper radar data. Curves for the same sounding have the same colour. Dark solid curves represent the arithmetic average of dropsonde data within the eyewall region. Maximum V_t is generally located well within the boundary layer, while the maximum V_r is often very close to the surface. The average height of the maximum tangential wind and maximum inflow during this time is 700 m and 180 m, respectively (see Table 1).

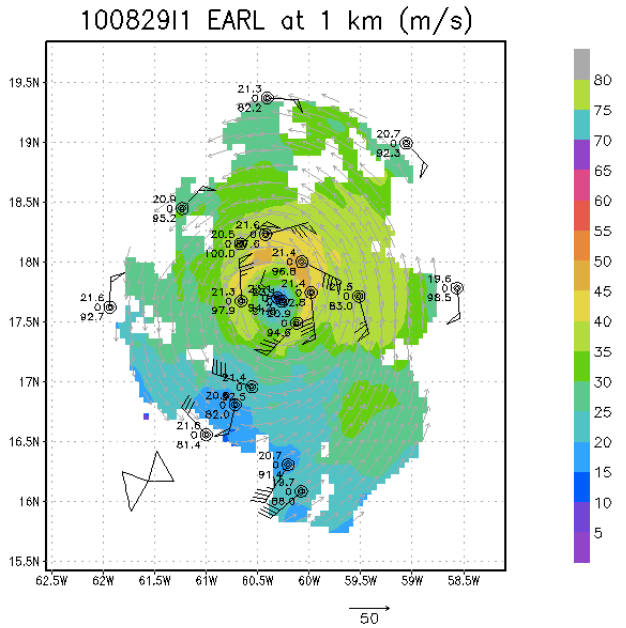

Figure 6. Doppler-radar derived wind vectors for hurricane Earl on 29 Aug (period 1) at a height of 1 km. The wind barbs from the dropwindsonde soundings at this level are superimposed. Doppler-derived wind speeds are color coded according to the scale on the right of the figure.

periods of interest, respectively. The eyewall region, and the associated radius of maximum tangential wind (RMW), is determined from the radar data as described in the foregoing subsection. In these figures, individual dropsondes within 10 km of the RMW are shown in colour while the thick black line is the arithmetical-mean vertical profile of the dropsondes. The full 10 m vertical resolution of dropsondes is being used here to plot the profiles shown.

Aside from the first set of vertical profiles before rapid intensification has commenced (Figure 7), the averaged profiles indicate that the maximum tangential wind speed occurs persistently deep within the vortex boundary layer as defined by the layer of strong inflow (Zhang *et al.* 2009, 2011, Smith *et al.* 2009). For example, Figure 8 shows that between 18 Z 29 Aug and 6Z 30 Aug, the maximum composite tangential wind occurs at a height of 400 m, where the mean inflow magnitude exceeds 15 m s^{-1}. Similarly, between 18 UTC 1 September and 6 UTC 2 September, the maximum composite tangential wind occurs at 500 m and the mean inflow exceeds 30 m s^{-1}! Between 6 UTC 2 September and 18 UTC 2 September, the composite tangential wind profile shows some weakening in intensity relative to the previous period, but the maximum tangential wind speed occurs at approximately 750 m where the mean inflow magnitude is still quite significant, 25 m s^{-1}. As discussed in prior and recent work (Willoughby 1995, Smith et al. 2009, Bui *et al.* 2009, Montgomery and Smith 2013), this layer of strong inflow is driven primarily the net radial pressure gradient brought about by surface friction.

The dropsonde data have the advantage of measuring boundary-layer structure with reasonably high vertical resolution (10 m). For a well-developed storm such as Earl, it is reasonable to assume that the pressure field in the boundary layer is to a first approximation axisymmetric. Then we can estimate the radial profile of pressure at each height by fitting a curve to the pressure observations at each drop location. Using this pressure profile, we may calculate the gradient wind at each analysis height, following that of Sanger *et al.* (2013), Bell and Montgomery (2008) and Kepert (2006a,b). Gradient wind balance is defined as a balance between the radial pressure gradient force per unit

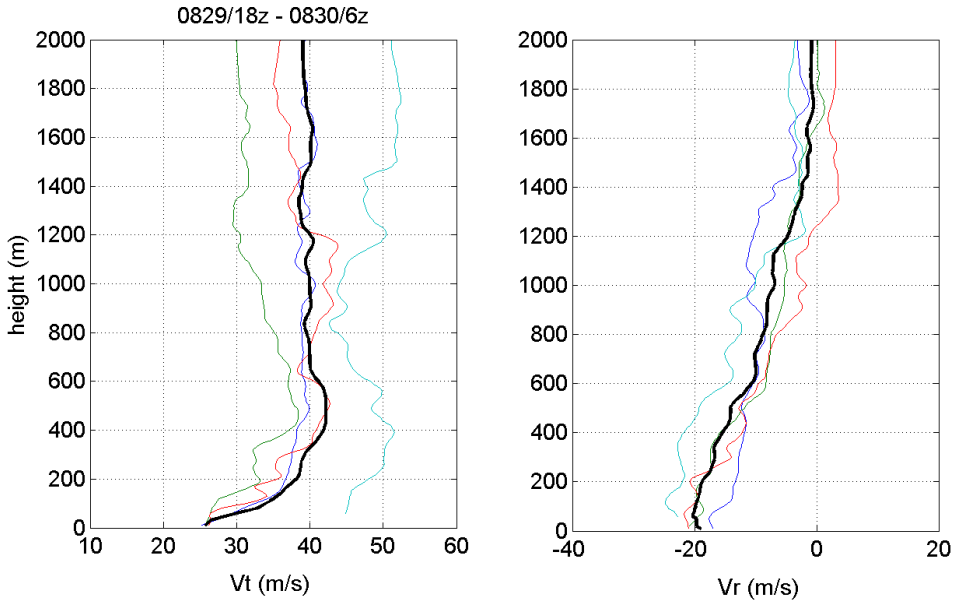

Figure 8. Vertical profiles of storm-relative tangential (V_t) and radial (V_r) wind composites and deviations thereto in the eyewall region of the vortex during the period 2: 0829/18Z - 0830/06Z. The eyewall region is defined as the region within 10 km from the RMW deduced using the Dopper radar data. Curves for the same sounding have the same colour. Dark solid curves represent the arithmetic average of dropsonde data within the eyewall region. Maximum V_t is generally located well within the boundary layer, while the maximum V_r is often very close to the surface. The average height of the maximum tangential wind and maximum inflow during this time is 570 m and 50 m, respectively, while the average height of the inflow layer is 1500 m (see Table 1).

mass and the sum of centrifugal and Coriolis forces:

$$\frac{1}{\rho}\frac{\partial p}{\partial r} = \frac{V_g^2}{r} + fV_g \qquad (1)$$

where V_g is the gradient wind. The gradient wind is obtained by solving the quadratic equation for V_g using the calculated radial pressure gradient as long as the radial pressure gradient remains positive.

Figures 11 and 12 show the results for the gradient wind calculations for the four periods at the height of the maximum tangential wind speed. The left panels show the observed pressure from individual sondes (blue circles) as a function of radius. Shown also are the best fit of the pressure data (red curve) in a polynomial form using a least square regression method. The right panels show the observed tangential wind in correspondence with each pressure observation. For comparison, the gradient wind is presented as a function of radius also (green curve). The red square in each right panel indicates the averaged value of V_t for the eyewall region. In this region, the average V_t is significantly higher than the corresponding gradient wind. Specifically, this average wind exceeds the gradient wind by 20% during period 1, 43% during period 2, 60% during period 3, and 32% during period 4. These calculations suggest that during both the rapid intensification and quasi-steady periods the boundary layer flow is significantly supergradient at the height of the maximum tangential wind speed. In contrast to the unbalanced state of affairs in the inner-core boundary layer, Figures 11 and 12 show that at outer radii the tangential winds are on average much closer to the gradient wind, albeit somewhat sub-gradient as is to expected where the radial advection of M is considerably weaker. At these radii, the boundary layer is more akin to that of a classical Ekman layer.

During spin up and maturity, the maximum tangential winds occur without exception within the layer of strong boundary layer inflow (< 1 km depth). The tangential winds near the radius of maximum wind in the boundary layer are persistently and significantly supergradient. For brevity, we have shown this feature only at the height of maximum tangential wind, but supporting analyses confirm this tendency throughout much of the boundary layer except very near the surface where the tangential winds become subgradient. The average maximum tangential wind speeds beneath the eyewall exceed the gradient wind by between 20% and 60%, with the largest excess occurring during the re-intensification period following the eyewall replacement on 2 September. As an indication of the inaccuracy of the gradient wind for characterizing the structure of the vortex in the boundary layer, the radius of the gradient wind maximum is up to three times the radius of the maximum observed tangential wind speed.

The data presented above offer a unique opportunity to assess the actual near-surface wind in terms of the gradient wind, which is predicted by Emanuel's potential intensity theory for a steady-state hurricane (E86, Emanuel 1995, Bister and Emanuel 1998, Emanuel 2004). The question is to what extent does Emanuel's potential theory for the gradient wind provide a measure for the total wind speed at the surface. Long ago, Carrier (1971 (and related investigations by Carrier *et al.* (1994) and refs.) predicted that the *total wind speed* in the boundary layer at any height is approximately equal to the gradient wind at the top of the boundary layer. Of course, according to the standard boundary-layer approximation the gradient wind is approximately uniform throughout the boundary layer. If true, the Carrier prediction would imply that Emanuel's potential intensity theory would be a good approximation to the near-surface wind, which is the preferred measure of intensity used by hurricane forecasters. Restricting attention to the rapid intensification and mature stages of the hurricane, i.e. Figures 8 and 9 and Figures 11d and 12b, it is

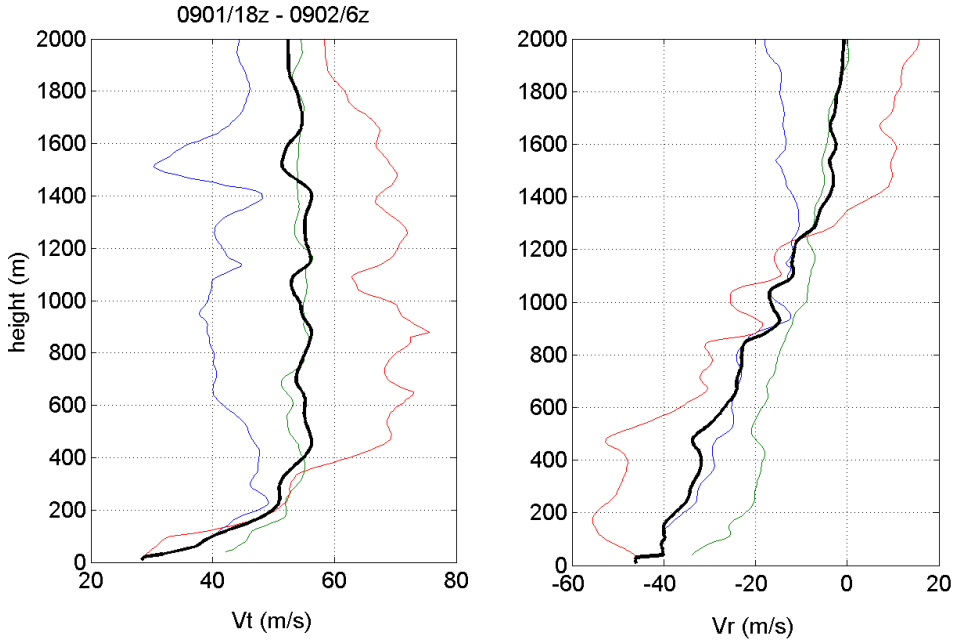

Figure 9. Vertical profiles of storm-relative tangential (V_t) and radial (V_r) wind composites and deviations thereto in the eyewall region of the vortex during the period 3: 0901/18Z - 0902/07Z. The eyewall region is defined as the region within 10 km from the RMW deduced using the Doppler radar data. Curves for the same sounding have the same colour. Dark solid curves represent the arithmetic average of dropsonde data within the eyewall region. Maximum V_t is generally located well within the boundary layer, while the maximum V_r is often very close to the surface. The average height of the maximum tangential wind and maximum inflow during this time is 450 m and 50 m, respectively, while the average height of the inflow layer is 1500 m (see Table I).

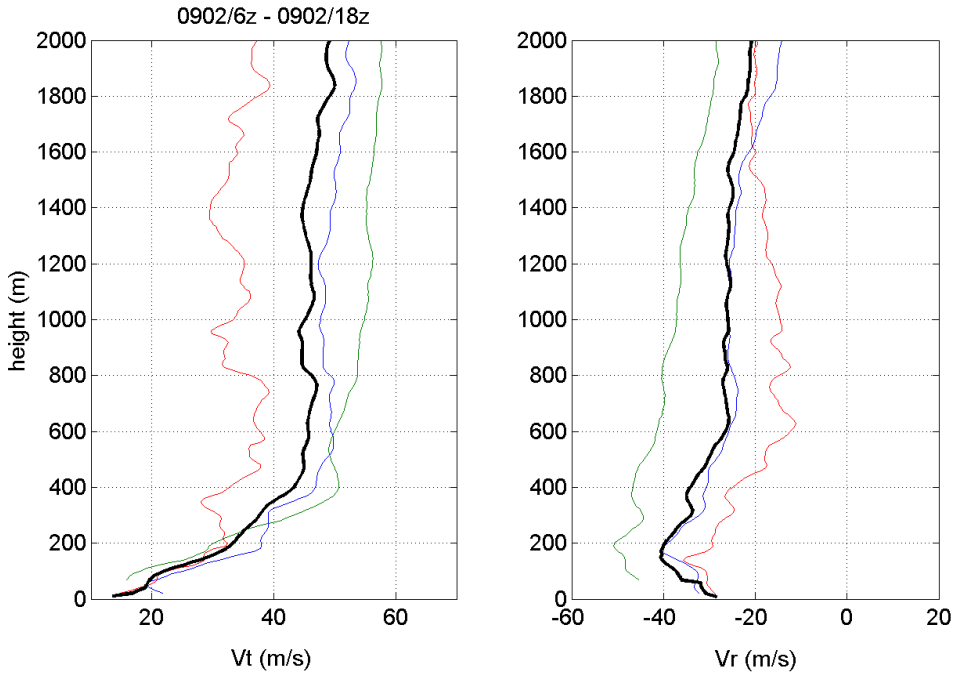

Figure 10. Vertical profiles of storm-relative tangential (V_t) and radial (V_r) wind composites and deviations thereto in the eyewall region of the vortex during the period 4: 0902/06Z - 0902/18Z. The eyewall region is defined as the region within 10 km from the RMW deduced using the Dopper radar data. Curves for the same sounding have the same colour. Dark solid curves represent the arithmetic average of dropsonde data within the eyewall region. Maximum V_t is generally located well within the boundary layer, while the maximum V_r is often very close to the surface. The average height of the maximum tangential wind and maximum inflow during this time is 1800 m and 10 m, respectively, while the average height of the inflow layer is above 2000 m (see Table I).

evident that the near-surface wind speed is approximately 33 m s^{-1} and 56 m s^{-1} compared with gradient wind speeds of 30 m s^{-1} and 36 m s^{-1} , respectively. Under these conditions the surface wind speeds are underestimated by 10% and 55%! Although the maximum gradient wind during these times is marginally larger, 33 m s^{-1} and 50 m s^{-1}, respectively, these maxima occur at a much larger radius than the maximum tangential wind speed in the

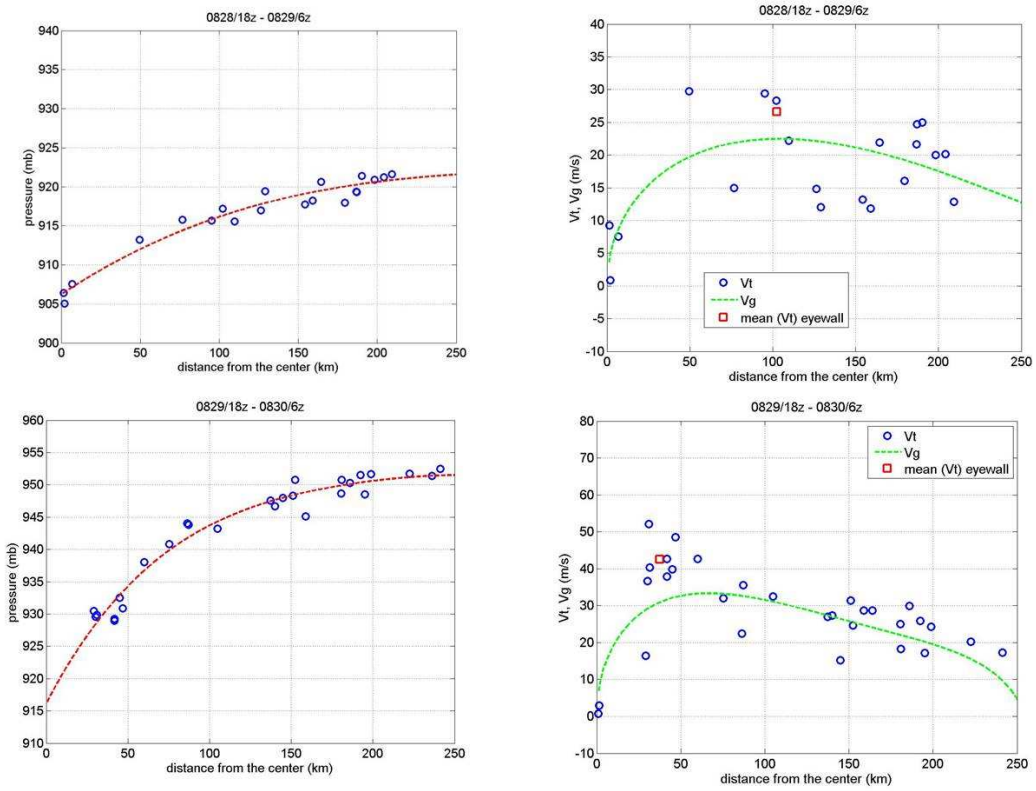

Figure 11. Gradient wind calculation at the height of maximum tangential wind speed (V_t) for periods 1 and 2 (Aug. 28 and Aug. 29). Left panels show dropsonde pressure observations (blue) as a function of radius with the fitted line (red) based on least square regression. Right panels show dropsonde observed V_t (blue) and gradient wind (V_g, green) as a function of radius. V_g is calculated using the pressure gradient by solving the gradient balance equation. The red square in the right panel is the average V_t at the eyewall region within 5 km from the radius of maximum wind speed.

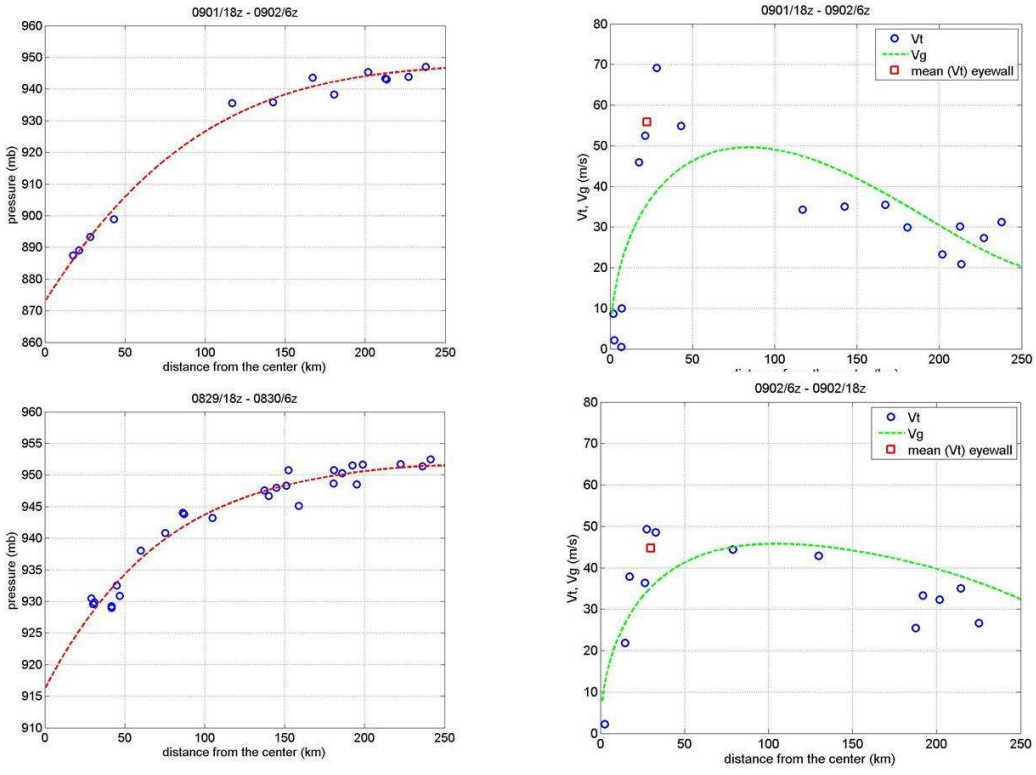

Figure 12. Gradient wind calculation at the height of maximum tangential wind speed (V_t) for periods 3 and 4 (Sept. 1 and Sept. 2). Left panels show dropsonde-observed pressure observations (blue) as a function of radius with the fitted line (red) based on least square regression. Right panels show dropsonde-observed V_t (blue) and gradient wind (V_g, green) as a function of radius. Here, V_g is calculated using the pressure gradient by solving the gradient balance equation (Eq.(1)). The red square in the right panel is the average V_t for the eyewall region within 5 km on either side of the RMW.

Period number	Average height of $V_{t_{max}}$ (m)	Average height of inflow layer (m)	Average height of peak inflow (m)	Average surface inflow angle	Percent negative $\partial\|V_r\|/\partial z$
1	700	700	180	12	25%
2	570	1500	50	35	80%
3	540	1800	10	46	50%
4	800	>2000	190	57	15%

Table I. Summary of boundary layer parameters for the eyewall region (within 10 km from the RMW) for periods 1, 2, 3 and 4 investigated in this study. These parameters include the average height of the maximum tangential wind speed, the average height of the inflow layer defined nominally as the height of 10% of the peak inflow, the average height of the peak inflow, the average of the near-surface inflow angle ($\tan^{-1}(-u/v)$), and the percentage of data where $\partial|V_r|/\partial z$ is negative below 200 m, where $|..|$ denotes magnitude and V_r denotes storm-relative radial velocity. The value for the inflow angle is the mean of the lowest 50 m data.

observations. Specifically, in the first case, the gradient wind maximum occurs at a radius of 70 km compared with 40 km for the observed tangential wind maximum (Figure 11d), while in the second case the gradient wind maximum occurs at 80 km compared with 25 km (Figure 12b).

The studies by Braun and Tao (2000) and Smith and Thomsen (2010) have elevated awareness of an important problem in the design of deterministic forecast models for hurricane intensity, namely which boundary-layer scheme is most appropriate? They provide estimates also of forecast uncertainty that follow from the uncertainty in not knowing the optimum boundary-layer scheme to use. In an effort to address this issue, Kepert (2012) compared a range of boundary-layer parameterization schemes in the framework of a steady-state boundary-layer model in which the tangential wind speed at the top of the boundary layer is prescribed and assumed to be in gradient wind balance. As a result of his analyses, he argues that boundary-layer schemes that do not reproduce a near-surface logarithmic layer are badly flawed and should not be used. However, Smith and Montgomery (2013b) present both observational and theoretical evidence that calls into question the existence of a near-surface logarithmic layer in the inner core of a tropical cyclone.

The observational data presented here offer a new opportunity to assess the foregoing issue in the high-wind region of the storm for both the composite boundary layer and individual vertical profiles. From the data shown, the composite tangential wind component in the boundary layer is a minimum at the surface. While the magnitude of the composite tangential wind generally increases with height near the surface, that of the composite mean radial velocity decreases with height, except in a relatively shallow layer above the sea surface during the intensification and mature stages. The shallow layer of increasing radial velocity magnitude is below 50 m during period 1, below 100 m during period 3 and below 200 m during the early weakening stage of period 4. Interestingly, a negative vertical gradient of composite mean radial velocity is evident throughout the boundary layer during period 2. During this period, the maximum mean inflow resides within 50 m from the surface. In those profiles where the radial wind speed increases slightly with height below approximately 100 m, we cannot definitively rule out the existence of a shallow log profile for the composite mean boundary layer structure. Nevertheless, for reasons given by Smith and Montgomery (2013b) we can rule out a strict log layer extending two hundred metres in depth as proposed by Powell (2003) for inferring drag coefficients at major hurricane wind speeds. However, for reasons given in Smith and Montgomery (2013b), the subsequent decrease in the magnitude of the radial wind component above this height is not consistent with a traditional log-layer. The data in Table I (last column) show that the percentage of eyewall soundings with a negative vertical gradient of the radial wind magnitude is up to 80 % (!), challenging the notion that there is always a shallow log layer in the inner core of a hurricane vortex (cf. Smith and Montgomery 2013b).

The observational data presented offer also an opportunity to examine the surface inflow angle and to compare these with previous observations and the predictions of different boundary layer schemes (Smith and Thomsen 2010). Surface inflow angles derived from recent observational studies of Hurricane Georges (1998), Hurricane Mitch (1998), Hurricane Danielle (1998) and Hurricane Isabel (2003) show maximum inflow angles of 24, 18, 24 and 26, respectively[2]. From their comparison with five different boundary layer schemes, Smith and Thomsen *op. cit.* found a range of inflow angle values between 17 and 35 ^{o} depending on the particular boundary layer scheme. However, from Table I, the average surface inflow angle in the eyewall region for the different observation periods of Earl show surface inflow angles of 12, 35, 46, 57^o, for periods 1,2,3 and 4, respectively. These values are consistent also with the composite analysis of surface inflow angle presented by Zhang and Uhlhorn (2012). These observations suggest that the boundary layer schemes studied by Smith and Thomsen are within the range of observed variability.

5.2. *Thermodynamic structure in the boundary layer*

As discussed in the Introduction, it is desired to learn more about the thermodynamics of the boundary layer and lower troposphere during the intensification process. In previous work we examined the inner-core and outer-core thermodynamic structure by simply binning the data into two radial groups, the eyewall region and the outer core region (Smith and Montgomery 2013a). We use now the data to construct radial profiles of boundary layer θ_e at both the 100 m and 1500 m levels. The results are shown in Figure 13 for three separate periods. At both levels, the increase of θ_e with decreasing radius is approximately

[2]The first of these angles is based on the right panels of the first and third rows of Figure 9 in Kepert (2006a), the second on panels (b) and (d) of Figure 6 in Kepert (2006b), the third from the second panels of each column of Figure 4 in Schwendike and Kepert (2008) and the fourth on the two right panels of Figure 19 in the same article.

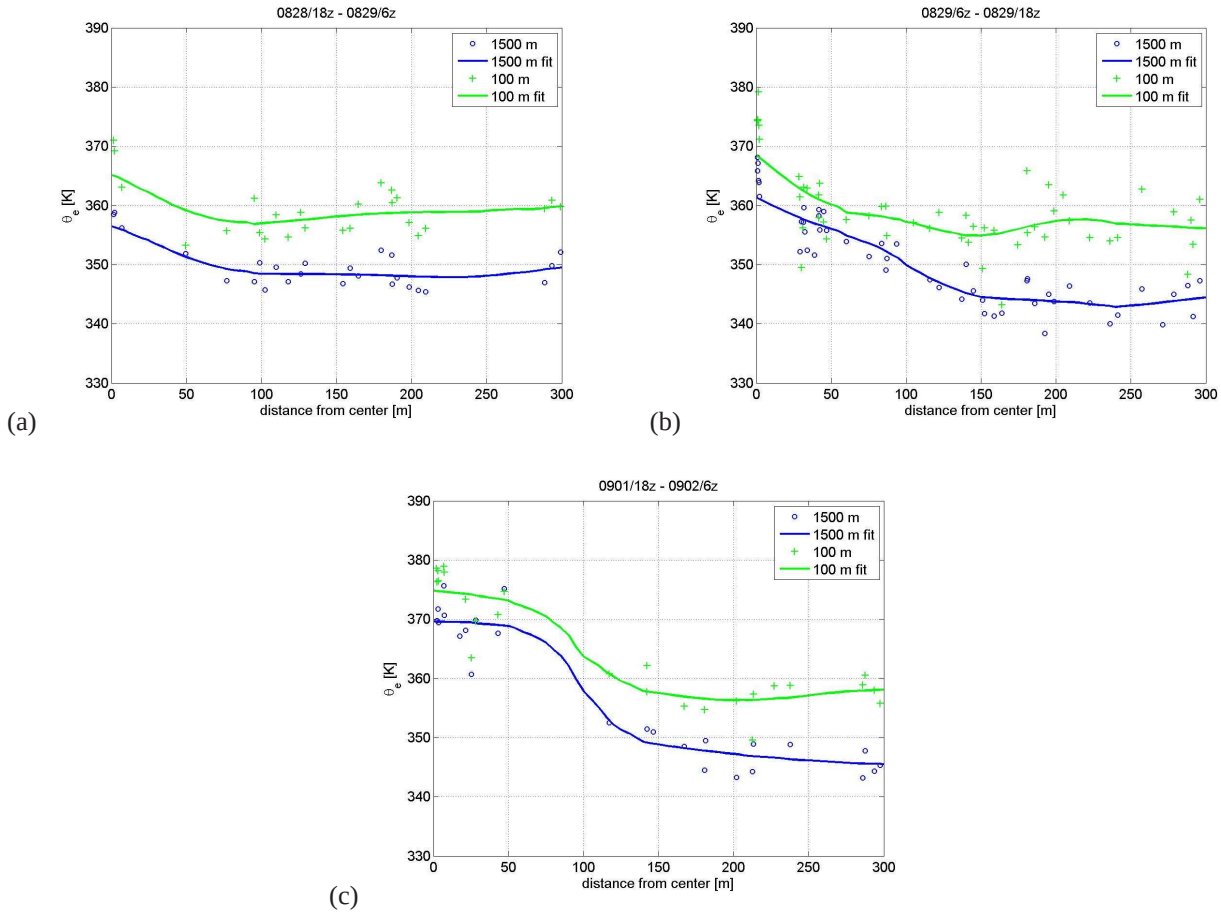

Figure 13. Values of θ_e at a height of 100 m and 1500 m as a function of radius.

monotonic within 150 km radius. The radial gradient of θ_e is relatively weak during the intensification phase, but becomes quite pronounced during the mature phase of the vortex evolution. At both levels, the difference between θ_e at the axis and 150 km radius increases from about 5 K to 20 K over the observation period.

As discussed in Montgomery *et al.* (2009) and Montgomery and Smith (2013), a radial increase in near-surface θ_e is necessary to maintain a degree of convective instability in the inner-core region in the presence of a developing warm core aloft during intensification. Early in the intensification period, the difference in θ_e between the heights 1500 m and 100 m is approximately 10 K outside of 150 km and this difference decreases to 8 K as one moves inwards to the nascent eyewall near 50 km radius. During the rapid intensification and mature period, the difference in θ_e between the heights 1500 m and 100 m is approximately 12 K outside of 150 km and this difference decreases to 5 K as one moves inwards to the RMW near the 25 km radius. During the re-intensification period after the eyewall replacement cycle, the difference is somewhat smaller, though the absence of data in this intermediate region cautions us against making quantitative statements.

In summary, the value of θ_e at 1.5 km altitude is consistently less than the corresponding near-surface value at all radii, even where the air is ascending into the eyewall. In the inner-most 150 km, the maximum difference is approximately 10 K, while the minimum is about 5 K. These observations suggest that the air going up into the eyewall has significantly lower values of θ_e than those near the surface. This finding is not consistent with the eruption of the boundary layer into the eyewall unless there are non-conservative processes acting to dilute the entropy of ascending air.

6. Conclusions

In this paper we have examined dynamic and thermodynamic aspects of Atlantic Hurricane Earl (2010) during its intensification and mature phases over four days of intensive measurements. The observations are based on a unique data set comprising airborne Doppler-radar and dropwindsondes released from the lower and upper troposphere during the collaborative NASA-GRIP and NOAA-IFEX field studies. These observational resources were supplanted with U.S. Air Force reconnaissance dropwindsonde data. The three and sometimes four aircraft that flew in Earl collected an observational data set that is perhaps the most extensive data set for an intensifying and mature hurricane ever. Here we use these observations to appraise elements of a new model for tropical-cyclone intensification articulated by Montgomery and Smith (2013).

The absolute angular momentum surfaces are shown to move progressively inwards over a deep layer as the storm intensifies. Also, the signature of the strengthening boundary layer inflow is evident by the increase in the upward-outward tilt of the M surfaces in the lower troposphere as these surfaces move inwards. During spin up and maturity, the maximum tangential winds persistently occur within the layer of strong boundary layer inflow

(< 1 km depth). The dropsonde composites show that the maximum radial inflow is very close to the sea surface, which is consistent with fluid dynamical considerations for a rapidly rotating vortex adjacent to a frictional boundary (e.g., Bödewadt 1940, also Schlichting 1968, Ch. 11).

The tangential winds near the radius of maximum wind in the boundary layer are persistently and significantly supergradient. For brevity, we have shown this only at the height of maximum tangential wind, but supporting analyses confirm this tendency throughout much of the boundary layer except very near the surface where the tangential winds become subgradient. The average maximum tangential winds beneath the eyewall exceed the gradient wind by between 20% and 60%, with the largest excess occurring during the re-intensification period following the eyewall replacement on 2 September. As an indication of the inaccuracy of the gradient wind for characterizing the structure of the vortex, the radius of the gradient wind maximum is up to three times the radius of the maximum observed tangential wind speed. At the radius of the observed tangential wind speed maximum, it is found that the maximum averaged surface wind speed is underestimated by the gradient wind speed.

The near-surface θ_e, and that at a height of 1.5 km increase approximately monotonically with decreasing radius within 150 km of the storm axis. The radial gradient of θ_e is relatively weak during the intensification phase, but becomes pronounced during the mature phase of the vortex evolution. Interestingly, the value of θ_e at 1.5 km altitude is consistently less than the corresponding near-surface value at all radii, even where the air is ascending into the eyewall. Specifically, in the inner-most 150 km, the maximum difference is approximatelly 10 K, while the minimum is about 5 K. The observations suggest that the air going up into the eyewall has significantly lower values of θ_e than those near the surface. This finding is not consistent with the eruption of the boundary layer into the eyewall unless there are non-conservative processes acting to dilute the entropy of ascending air.

The findings herein complement recent observational work of Sanger *et al.* (2013) and provide further support for the new paradigm of tropical cyclone intensification.

7. Acknowledgements

We acknowledge NASA and Ramesh Kakar for their support of the GRIP experiment. MTM acknowledges the support of NSF AGS-0733380 and NASA grants NNH09AK561, NNG11PK021 and NNG09HG031. JAZ acknowledges the support from NOAA's Hurricane Forecast and Improvement Program (HFIP). We want to thank Sim Aberson and Sylvie Lorsolo for providing the radar composite data for each Earl flight. JAZ is grateful also to Robert Rogers and Paul Reasor for helpful discussions.

8. References

Bister M Emanuel KA. 1998: Dissipative heating and hurricane intensity. *Meteor. Atmos. Phys.*, **65,** 233-240.

Bell MM Montgomery MT. 2008: Observed structure, evolution, and potential intensity of Category 5 Hurricane Isabel (2003) from 12 to 14 September. *Mon. Wea. Rev.*, **65**, 2025-2046.

Bödewadt UT 1940 Die Drehstroemung über festem Grund. *ZAMM*, **20**, 241-253

Braun SA Tao W-K. 2000: Sensitivity of high-resolution simulations of Hurricane Bob (1991) to planetary boundary layer parameterizations. *Mon. Wea. Rev.*, **128**, 3941-3961.

Bui HH Smith RK Montgomery MT Peng J. 2009 Balanced and unbalanced aspects of tropical-cyclone intensification. *Q. J. R. Meteorol. Soc.*, **135,** 1715-1731.

Carrier, GF, Hammond, AL, and George, OD. 1971 A model of the mature hurricane. *J. Fluid Mech.*, **47**, 145–170.

Carrier, G.F., Fendell, F., Mitchell, J. and Bronstein, M. 1994 Self-sustaining intense vortices. *Physica D*, **77**, 77–96.

Charney JG Eliassen A. 1964 On the growth of the hurricane depression. *J. Atmos. Sci.*, **21**, 68-75.

Elsberry R Harr P. 2008: Tropical cyclone structure (TCS08) Field experiment scientific basis, observational platforms, and strategy. Asia-Pacific Journal of Atmospheric Sciences, **44**, 1-23.

Emanuel KA. 1986: An air-sea interaction theory for tropical cyclones. Part I: Steady state maintenance. *J. Atmos. Sci.*, **43**, 585-604.

Emanuel KA. 1988: The maximum intensity of hurricanes. *J. Atmos. Sci.*, **45,** 1143-1155.

Emanuel KA. 1994: *Atmospheric convection.* Oxford University Press, 580pp.

Emanuel KA. 1995: Sensitivity of tropical cyclones to surface exchange coefficients and a revised steady-state model incorporating eye dynamics. *J. Atmos. Sci.*, **52**, 3969-3976.

Emanuel, KA. 1997: Some aspects of hurricane inner-core dynamics and energetics. *J. Atmos. Sci.*, **54**, 1014-1026.

Emanuel KA. 2003: Tropical Cyclones. *Annu. Rev. Earth Planet. Sci.*, **31**, 75-104.

Emanuel KA. 2004: Tropical Cyclone Energetics and Structure. In *Atmospheric Turbulence and Mesoscale Meteorology*, E. Fedorovich, R. Rotunno and B. Stevens, editors, Cambridge University Press, pp280.

Emanuel KA Rotunno R. 2011: Self-stratification of tropical cyclone outflow. Part I: Implications for storm structure. *J. Atmos. Sci.*, **68**, 2236-2249.

Emanuel KA Neelin JD Bretherton CS. 1994: On large-scale circulations in convecting atmospheres. *Q. J. R. Meteorol. Soc.*, **120**, 1111-1143.

Franklin JL Lord SJ Feuer SE and Marks FD. 1993: The Kinematic Structure of Hurricane Gloria (1985) Determined from Nested Analyses of Dropwindsonde and Doppler Radar Data. *Mon. Wea. Rev.*, **121**, 2433-2451.

Franklin JL Black ML and Valde K. 2003: GPS dropwindsonde wind profiles in hurricanes and their operational implications. *Wea. Forecasting*, **18**, 32C44.

Gamache JF. 1997: Evaluation of a fully three-dimensional variational Doppler analysis technique. Preprints, 28th Conf. on Radar Meteorology, Austin, TX, Amer. Meteor. Soc., 422-423.

Gamache, J. F., cited 2012: Real-time dissemination of hurricane wind fields determined from airborne Doppler radar data. National Hurricane Center. [Available online at http://www.nhc.noaa.gov/jht/2003-2005reports/DOPLRgamache_JHTfinalreport.pdf]

Hawkins HF and Imbembo SM. 1976: The structure of a small, intense hurricane, Inez (1966). *Mon. Wea. Rev.*, **104**, 418-442.

Hock TF and Franklin JL. 1999: The NCAR GPS dropwindsonde. *Bull. Amer. Meteor. Soc.*, **80**, 407C420.

Kepert JD. 2006a Observed boundary-layer wind structure and balance in the hurricane core. Part I. Hurricane Georges. *J. Atmos. Sci.*, **63,** 2169-2193.

Kepert JD. 2006b Observed boundary-layer wind structure and balance in the hurricane core. Part II. Hurricane Mitch. *J. Atmos. Sci.*, **63,** 2194-2211.

Kepert JD. 2012 Choosing a boundary-layer parameterisation for tropical cyclone modelling. *Mon. Wea. Rev.*, **140**, 1427-1445.

Marks F Houze RA and Gamache JF. 1992: Dual-aircraft investigation of the inner core of Hurricane Norbert. Part I: Kinematic structure. *J. Atmos. Sci.*, 49, 919942.

Marks FD Black PG Montgomery MT Burpee RW. 2008: Structure of the Eye and Eyewall of Hurricane Hugo (1989). *Mon. Wea. Rev.*, , **136**, 1237-1259.

Montgomery MT Bell MM Aberson SD Black ML. 2006: Hurricane Isabel (2003): New insights into the physics off intense storms. Part I. Mean vortex structure and maximum intensity estimates. *Bull. Amer. Meteor. Soc.*, *87*,1335-1347.

Montgomery MT Nguyen SV Smith RK Persing J. 2009: Do tropical cyclones intensify by WISHE? *Q. J. R. Meteorol. Soc.*, **135,** 1697-1714.

Montgomery MT Smith RK. 2013 Paradigms for tropical-cyclone intensification. *Aust. Meteor. Ocean. Journl.*, (in press).

Nguyen SV Smith RK Montgomery MT. 2008 Tropical-cyclone intensification and predictability in three dimensions. *Q. J. R. Meteorol. Soc.*, **134**, 563-582.

Ooyama KV. 1964 A dynamical model for the study of tropical cyclone development. *Geophys. Int.*, **4,** 187-198.

Ooyama KV. 1969 Numerical simulation of the life cycle of tropical cyclones. *J. Atmos. Sci.*, **26**, 3-40.

Ooyama KV. 1982 Conceptual evolution of the theory and modeling of the tropical cyclone. *J. Meteor. Soc. Japan*, **60,** 369-380.

Powell MD Vickery PJ and Reinhold TA 2003: Reduced drag coefficient for high wind speeds in tropical cyclones. *Nature*, **422**, 279-283.

Reasor, P. D., M. Eastin, and J. F. Gamache, 2009: Rapidly intensifying Hurricane Guillermo (1997). Part I: Low-wavenumber structure and evolution. *Mon. Wea. Rev.*, , **137**, 603C631.

Reasor, P. D., and M. D. Eastin, 2012: Rapidly intensifying Hurricane Guillermo (1997). Part II: Resilience in shear. *Mon. Wea. Rev.*, , **140**, 425C444.

Reasor, P. D., R. Rogers, and S. Lorsolo, 2013: Environmental flow impacts on tropical cyclone structure diagnosed from airborne Doppler radar compoisites. *Mon. Wea. Rev.*, in review.

Sanger N. 2011 An Observational Study of Tropical Cyclone Spinup in Supertyphoon Jangmi and Hurricane Georges. Ph.D. Dissertation. U.S. Naval Postgraduate School. Monterey, California, 120 pp.

Sanger NT, Montgomery MT, Smith RK, Bell MM. 2012 An observational study of tropical-cyclone spin-up in Supertyphoon Jangmi (2008) from 24 - 27 September. *Mon. Wea. Rev.*, accepted with revision.

Schlichting, H. 1968 Boundary-Layer Theory. 6th ed. McGraw-Hill, 748 pp.

Schwendike J Kepert JD. 2008 The boundary layer winds in Hurricane Danielle 1998 and Hurricane Isabel 2003. *Mon. Wea. Rev.*, **136**, 3168-3192.

Shapiro LJ Montgomery MT. 1993 A three-dimensional balance theory for rapidly-rotating vortices. *J. Atmos. Sci.*, **50**, 3322-3335.

Smith RK Montgomery MT and Vogl S. 2008: A critique of Emanuel's hurricane model and potential intensity theory. *Q. J. R. Meteorol. Soc.*, **134**, 551-561.

Smith RK Montgomery MT Nguyen SV. 2009 Tropical-cyclone spin up revisited. *Q. J. R. Meteorol. Soc.*, **135,** 1321-1335.

Smith RK Montgomery MT. 2010 Hurricane boundary-layer theory. *Q. J. R. Meteorol. Soc.*, **136**, 1665-1670.

Smith RK Thomsen GL. 2010 Dependence of tropical-cyclone intensification on the boundary-layer representation in a numerical model. *Q. J. R. Meteorol. Soc.*, **136**, 1671-1685.

Smith RK Montgomery MT. 2013a How important is the isothermal expansion effect in elevating equivalent potential temperature in the hurricane inner core? *Q. J. R. Meteorol. Soc.*, **139** 70-74.

Smith RK Montgomery MT. 2013b On the existence of the logarithmic surface layer in hurricanes. *Q. J. R. Meteorol. Soc.*, (in press).

Willoughby HE. 1988 The dynamics of the tropical cyclone core. *Aust. Met. Mag.*, **36**, 183-191.

Willoughby HE. 1995 Mature structure and evolution. In *Global Perspectives on Tropical Cyclones. pp21-62. WMO/TD-No 693 (Ed. R. L. Elsberry), World Meteorological Organization, Geneva*, 289pp.

Willoughby HE and Chelmow M., 1982: Objective determination of hurricane tracks from aircraft observations. *Mon. Wea. Rev.*, , **110**,198-1305.

Zhang D-L Liu Y Yau MK. 2001 A multi-scale numerical study of Hurricane Andrew (1992). Part IV: Unbalanced flows. *Mon. Wea. Rev.*, **129**, 92-107.

Zhang JA and Uhlhorn EW 2012: Hurricane sea-surface inflow angle and an observation-based parametric model of the two-dimensional surface wind field. *Mon. Wea. Rev.*, , **140**, 3587-3604.

Zhang JA Drennan WM Black PG and French JR 2009: Turbulence structure of the hurricane boundary layer between the outer rainbands. *J. Atmos. Sci.*, **66**, 2455-2467.

Zhang JA Rogers RF Nolan DS and Marks FD 2011: On the characteristic height scales of the hurricane boundary layer. *Mon. Wea. Rev.*, , **139**, 2523-2535.